Combined measurement of velocity and temperature in liquid metal convection

Till Zürner[1],†, **Felix Schindler**[2], **Tobias Vogt**[2], **Sven Eckert**[2]
and Jörg Schumacher[1]

[1]Institute of Thermodynamics and Fluid Mechanics, Technische Universität Ilmenau, Postfach 100565,
D-98684 Ilmenau, Germany

[2]Department of Magnetohydrodynamics, Institute of Fluid Dynamics, Helmholtz-Zentrum Dresden –
Rossendorf, Bautzner Landstraße 400, D-01328 Dresden, Germany

Combined measurements of velocity components and temperature in a turbulent
Rayleigh–Bénard convection flow at a low Prandtl number of $Pr = 0.029$ and Rayleigh
numbers of $10^6 \leqslant Ra \leqslant 6 \times 10^7$ are conducted in a series of experiments with durations
of more than a thousand free-fall time units. Multiple crossing ultrasound beam lines
and an array of thermocouples at mid-height allow for a detailed analysis and
characterization of the complex three-dimensional dynamics of the single large-scale
circulation roll in a cylindrical convection cell of unit aspect ratio which is filled with
the liquid metal alloy GaInSn. We measure the internal temporal correlations of the
complex large-scale flow and distinguish between short-term oscillations associated
with a sloshing motion in the mid-plane as well as varying orientation angles of
the velocity close to the top/bottom plates and the slow azimuthal drift of the mean
orientation of the roll as a whole that proceeds on a time scale up to a hundred
times slower. The coherent large-scale circulation drives a vigorous turbulence in the
whole cell that is quantified by direct Reynolds number measurements at different
locations in the cell. The velocity increment statistics in the bulk of the cell displays
characteristic properties of intermittent small-scale fluid turbulence. We also show that
the impact of the symmetry-breaking large-scale flow persists to small-scale velocity
fluctuations thus preventing the establishment of fully isotropic turbulence in the cell
centre. Reynolds number amplitudes depend sensitively on beam-line position in the
cell such that different definitions have to be compared. The global momentum and
heat transfer scalings with Rayleigh number are found to agree with those of direct
numerical simulations and other laboratory experiments.

Key words: Bénard convection, turbulent convection

---

1. Introduction

The understanding of transport processes in several turbulent convection flows in
nature and technology can be improved by means of Rayleigh–Bénard convection
(RBC) studies at very low Prandtl numbers of $Pr \ll 10^{-1}$. Prominent examples

† Email address for correspondence: till.zuerner@tu-ilmenau.de

are stellar and solar convection (Spiegel 1962), the geodynamo in the core of the Earth (Christensen & Aubert 2006), the blanket design in nuclear fusion reactors (Salavy *et al.* 2007) and liquid metal batteries for renewable energy storage (Kelley & Weier 2018). Laboratory experiments in turbulent RBC at low Prandtl numbers are, however, notoriously challenging since they have to rely on liquid metals as working fluid to obtain a sufficiently high thermal diffusivity in comparison to the kinematic viscosity. Liquid metals are opaque and thus exclude optical imaging by means of particle image velocimetry (Adrian & Westerweel 2011) or Lagrangian particle tracking (Hoyer *et al.* 2005; Toschi & Bodenschatz 2009). The analysis relies instead on ultrasound Doppler velocimetry (UDV) (Takeda 1987) in combination with local temperature measurements. We mention here pioneering experiments by Takeshita *et al.* (1996), Cioni, Ciliberto & Sommeria (1997), Mashiko *et al.* (2004) and Tsuji *et al.* (2005) and more recently by Khalilov *et al.* (2018), or Vogt *et al.* (2018*a*), who found a jump-rope-type large-scale flow.

In closed convection cells, a large-scale circulation (LSC) builds up that affects the way and amount of heat and momentum carried across the turbulent fluid (Ahlers, Grossmann & Lohse 2009; Chillà & Schumacher 2012). Its complex three-dimensional shape and dynamics have been studied intensively in the past decade for RBC flows with $Pr > 0.1$, for example in theoretical oscillator models (Brown & Ahlers 2009), experiments (Funfschilling & Ahlers 2004; Sun, Xia & Tong 2005; Xi *et al.* 2009; Zhou *et al.* 2009) and direct numerical simulations (Stevens, Clercx & Lohse 2011; Shi, Emran & Schumacher 2012). The low-Prandtl-number regime has been largely unexplored with respect to the large-scale flow dynamics. Only recently has the interest in this research topic increased with new experiments by Khalilov *et al.* (2018) and Vogt *et al.* (2018*a*). The typical cylindrical cell shape leads to a statistical symmetry of convective turbulence with respect to the azimuthal direction and opens the possibility of complex LSC dynamics. These consist of shorter-term oscillations of the mean flow orientation close to the plates which point in different directions at top and bottom. The oscillations can be superimposed by a slow azimuthal drift of the mean flow orientation of the LSC roll as a whole. The UDV technique has been shown to be able to detect complex flow structures in liquid metal thermal convection (Mashiko *et al.* 2004; Tsuji *et al.* 2005; Vogt *et al.* 2018*a*,*b*). This method has been extended recently to linear transducer arrays that allow the reconstruction of two-dimensional flow patterns at high spatial and temporal resolution (Franke *et al.* 2013).

In this work, we report multi-technique long-term measurements of a fully turbulent convection flow in the liquid metal alloy gallium–indium–tin (GaInSn; $Pr = 0.029$) in a closed cylindrical cell of aspect ratio 1. We combine 10 UDV beam lines and 11 thermocouples for an in-depth analysis of the LSC at Rayleigh numbers $Ra \leqslant 6 \times 10^7$. Multiple crossing UDV beam lines close to the bottom/top walls and at the mid-plane in combination with an array of thermocouple probes arranged in a semicircle of high angular resolution at half-height enable the detailed experimental reconstruction of a short-term oscillatory torsional motion of the LSC at top and bottom, the sloshing motion at half-height and the superposition of this short-term dynamics with a slow azimuthal drift. The LSC flow is found to be more coherent as in comparable RBC flows at higher Prandtl numbers, agreeing also with recent direct numerical simulations (DNS) by Scheel & Schumacher (2016, 2017) in the same parameter range. Our analysis reveals a LSC roll with large inertia, able to drive a vigorous fluid turbulence in the bulk. This is motivated by a recent DNS study where the higher inertia of fluid turbulence in low-Prandtl-number fluids is found to
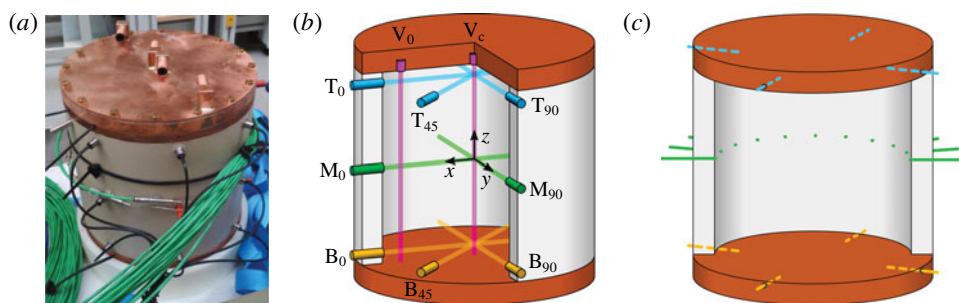
FIGURE 1. (Colour online) Convection cell design and arrangement of ultrasound beam lines and thermocouples. (*a*) Photograph. (*b*) Positions and labels of the UDV sensors. The subscripts of the labels refer to the azimuthal position in degrees. (*c*) Positions of the temperature sensors. The cylindrical convection cell is thermally insulated during the experiment.

be largely caused by the injection of turbulent kinetic energy at a larger scale due to the coarser thermal plumes comprising the LSC (Schumacher, Götzfried & Scheel 2015). A reverse influence of the small-scale turbulence on the large-scale flow is, however, also possible as extreme dissipation events may trigger LSC reorientations (Schumacher & Scheel 2016). We investigate the turbulent character of the flow from direct determination of the Reynolds number dependence $Re(Ra)$ in the cell centre using UDV. On the basis of this measurement method, we also analyse the statistics of velocity increments and the isotropy of small-scale turbulence in this liquid metal flow. Our experiment yields time series of velocity components and temperature of almost 2000 free-fall time units. Although three-dimensional high-resolution DNS of such flows provide the full information of the turbulent fields, they cannot be run for extended time intervals of a few hundred free-fall time units or even more (van der Poel, Stevens & Lohse 2013; Scheel & Schumacher 2016, 2017). Laboratory experiments are currently the only way to conduct a long-term global analysis of three-dimensional LSC flow that has to be considered as a superposition of different modes with different typical time scales.

The outline of the paper is as follows. In § 2 we present details of the experiment. Section 3 is dedicated to the large-scale flow in the cell. We discuss the oscillation of the azimuthal orientation, the torsion as well as the sloshing modes by means of three representative runs at $Ra = 10^6$, 10^7 and 6×10^7. For the latter, we study a cessation event in detail. Furthermore, we take a closer look at the internal temporal correlations of the large-scale flow. Section 4 reviews the global transport of heat and momentum. Section 5 provides our findings for the statistics of the velocity increments. We close the work with a final summary and give a brief outlook into future work. The values of selected quantities of the presented experiments are given in the supplementary material (https://doi.org/10.1017/jfm.2019.556).

2. Experimental set-up

The cylindrical convection cell (figure 1a) has an inner diameter $D = 2R = 180$ mm and an inner height $H = 180$ mm with aspect ratio $\Gamma = D/H = 1$. The sidewalls are made of polyether ether ketone (PEEK), and the top and bottom plates consist of copper with a thickness of 25 mm. The top plate is cooled with water supplied by

a thermostat. A ceramic heating plate with a diameter of 190 mm is mounted below the bottom copper plate, supplying a maximum heating power of 2 kW for a DC voltage of 230 V. The cell is filled with the eutectic alloy GaInSn (melting point of 10.5 °C). At a mean temperature $\bar{T}$ of 35 °C, the melt has a Prandtl number of $Pr = 0.029$. The properties of GaInSn are then: mass density $\rho = 6.3 \times 10^3$ kg m^{-3}, kinematic viscosity $\nu = 3.2 \times 10^{-7}$ m^2 s^{-1}, thermal diffusivity $\kappa = 1.1 \times 10^{-5}$ m^2 s^{-1}, thermal conductivity $\lambda = 24.3$ W (K m)$^{-1}$ and volumetric expansion coefficient $\alpha = 1.2 \times 10^{-4}$ K^{-1} (Müller & Bühler 2001; Plevachuk *et al.* 2014). The Rayleigh number varies in the range $10^6 \leqslant Ra \leqslant 6 \times 10^7$ thus covering almost two orders of magnitude. The mean fluid temperature is held at about 35 °C for all experiments, except for the highest temperature differences at $Ra \sim 6 \times 10^7$. There, due to limited cooling power, $\bar{T}$ rises to 40 °C resulting in $Pr = 0.028$.

The velocity measurements rely on the pulsed UDV technique applying a specific configuration (figure 1b), where 10 transducers emit ultrasonic pulses with a frequency of 8 MHz along a straight beam line and record the echoes that are reflected by small particles in the fluid. Knowing the speed of sound in GaInSn allows us to determine the spatial particle position along the ultrasound propagation from the detected time delay between the burst emission and the echo reception. The movement of the scattering particles, which are always present in a GaInSn melt, results in a small time shift of the signal structure between two successive bursts from which the velocity can be calculated.

The plate temperatures are measured as the average from four K-thermocouples distributed in 90° intervals around the plate circumference (dashed lines in figure 1c). Eleven additional thermocouples are arranged at half the height of the convection cell in a semicircle in steps of 18° (solid lines in figure 1c). They span the azimuthal interval of $157.5° < \phi < 337.5°$, where $\phi = 0°$ is the positive x-axis (see figures 1b and 2).

The global heat flux $\dot{Q}$ is determined at the top plate: the inflowing cooling water of temperature T_{in} heats up to a temperature T_{out} at the outlet. In combination with the water volume flux $\dot{V}$ the extracted heat flux is $\dot{Q}_{cool} = \tilde{c}_p \tilde{\rho} \dot{V}(T_{out} - T_{in})$ with $\tilde{c}_p$ and $\tilde{\rho}$ being the isobaric heat capacity and mass density, respectively, of the cooling water at its mean temperature $(T_{in} + T_{out})/2$ (Çengel 2008). Only measurements with $T_{out} - T_{in} > 0.2$ K are considered due to the incertitude of the thermocouples.

Heat losses to the environment are minimized by insulating the experiment with Styrofoam and placing it on a polyamide base with a thermal conductivity ~ 0.23 W (m K)$^{-1}$. Any remaining heat losses through the sidewall are determined by measuring the radial temperature gradient $\partial_r T$ within the sidewall. Three pairs of thermocouples are distributed at 120° intervals around the circumference at half the height of the cell. The vertical position is taken as representative of the average heat loss over the cell height and the three azimuthal positions are to minimize anisotropic effects caused by the LSC. The radial heat flux is given by $\dot{Q}_{loss} = -\lambda_{sidewall} \pi DH \partial_r T$ with $\partial_r T$ as the average value of all three measurement positions, πDH as the inner sidewall surface and $\lambda_{sidewall} = 0.25$ W (K m)$^{-1}$. The calculated heat loss $\dot{Q}_{loss}$ is, ideally, the difference between the heating power $\dot{Q}_{heat}$ supplied at the bottom and the cooling power extracted at the top of the cell $\dot{Q}_{loss} = \dot{Q}_{heat} - \dot{Q}_{cool}$. To calculate the average heat flux $\dot{Q} = (\dot{Q}_{heat} + \dot{Q}_{cool})/2$ through the cell, the measured cooling power is corrected by half of the radial heat losses: $\dot{Q} = \dot{Q}_{cool} + \dot{Q}_{loss}/2$.
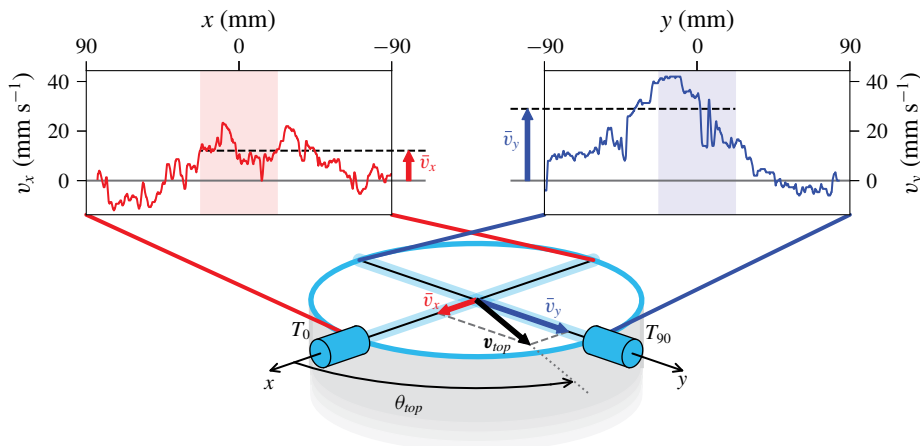
FIGURE 2. (Colour online) Calculation of the orientation angle θ_{top} of the large-scale flow close to the top plate. The UDV sensor T_0 at $\phi = 0°$ measures the radial v_x profile (left) and T_{90} at $\phi = 90°$ measures the radial v_y profile (right). The mean velocities $\bar{v}_x$ and $\bar{v}_y$ are determined over the central shaded profile intervals. These values are used as components of the horizontal velocity vector of the LSC which is denoted as $\boldsymbol{v}_{top}$.

3. Large-scale flow dynamics

3.1. *Long-term dynamics of the large-scale flow structure*

We now discuss the long-time evolution of the LSC for a measurement at our highest Rayleigh number $Ra = 6 \times 10^7$. Times are given in units of the free-fall time $\tau_{ff} = \sqrt{H/(g\alpha\Delta T)}$. Variable g is the acceleration due to gravity. For the example data set at $Ra = 6 \times 10^7$, the free-fall time is $\tau_{ff} = 2.3$ s and the total duration of the time series is $1700\tau_{ff}$. Figure 2 illustrates how the orientation angle of the flow in the centre close to the top plate is calculated. The velocity profiles $v_x(x, t)|_{y=0}$ and $v_y(y, t)|_{x=0}$ are measured by UDV sensors T_0 and T_{90}, respectively, 10 mm below the top plate. At the central crossing point of the ultrasonic beams the horizontal velocity vector $\boldsymbol{v}_{top} = (\bar{v}_x, \bar{v}_y)$ and the resulting orientation angle are given by

$$\bar{v}_i(t) = \langle v_i(i, t)\rangle_{-D/8 \leqslant i \leqslant D/8}, \quad \text{and thus} \quad \theta_{top} = \arctan\left(\frac{\bar{v}_y}{\bar{v}_x}\right), \qquad (3.1)$$

with $i = x, y$. The orientation angle at the bottom plate θ_{bot} is calculated analogously using UDV sensors B_0 and B_{90}. Figure 3(a) shows a time series of $\theta_{top} + 180°$ and θ_{bot}. The two angles match very well which implies that in this measurement they always maintain a mean azimuthal offset of $180°$. This validates the presence of a single coherent LSC roll in the cell. Figure 3(f,h) presents a detailed view of the data in figure 3(a). It can now be seen that the orientation angles oscillate around a common mean at an oscillation time of $\tau_{osc} \sim 10\tau_{ff}$. Furthermore, the angles oscillate in anti-phase, which is a clear indication of the torsion mode (Funfschilling & Ahlers 2004; Xie, Wei & Xia 2013; Khalilov *et al.* 2018). The LSC flow is thus characterized by a torsion in agreement with DNS at similar Pr by Scheel & Schumacher (2016, 2017) and experiments in liquid sodium at $Pr = 0.0094$ (Khalilov *et al.* 2018). We come back to this point in § 3.2. Figure 3(a) shows clearly the additional slow drift of the mean orientation angle by more than $180°$ over the full measurement time period
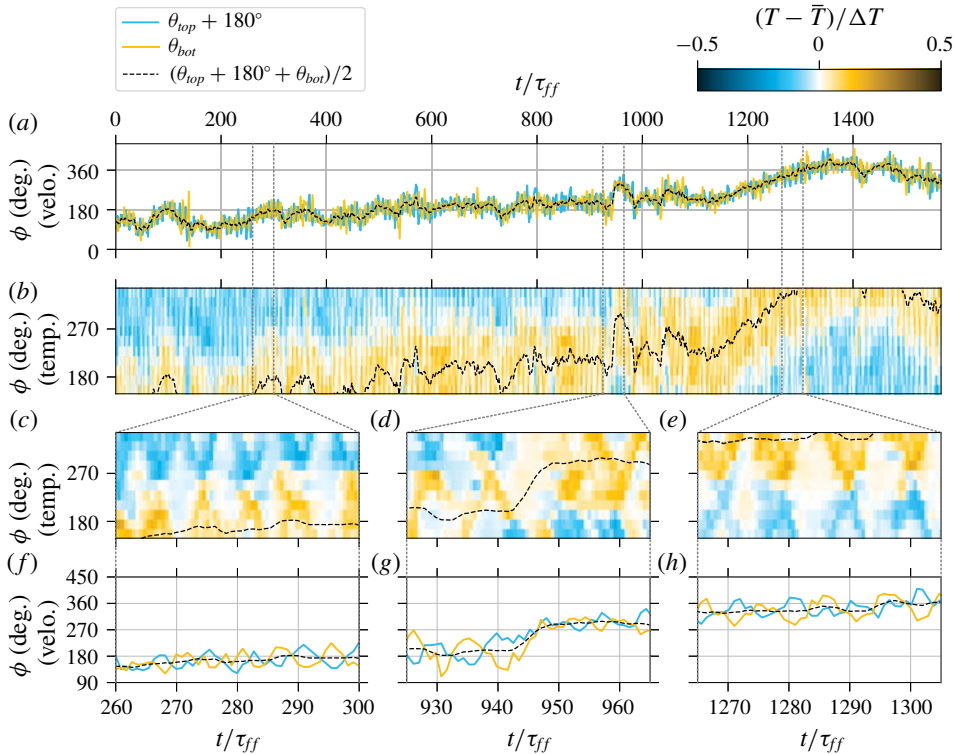
FIGURE 3. Large-scale flow structure for $Ra = 6 \times 10^7$ ($\tau_{ff} = 2.3$ s) measured by UDV sensors near the plates (velo.) and thermocouples at mid-height (temp.). (a) The LSC orientation angles at the top (θ_{top}) and bottom (θ_{bot}) plates (see figure 2). The black dashed line is the smoothed average of the top and bottom angles. (b) Temperatures near the wall at half the height of the cell over time and azimuthal position ϕ. The dashed black line is identical to the one in (a). (c–e) Detailed views of time series (b) for a time interval of $40\tau_{ff}$. (f–h) Detailed views of time series (a) for same time interval.

of $\tau_{total} \approx 1700\tau_{ff}$, a motion that is due to the statistical azimuthal symmetry in the cylindrical set-up. The characteristic time scale τ_{drift} of this motion can be estimated to be of the order of the thermal diffusion time scale $\tau_{drift} \sim \tau_\kappa = H^2/\kappa$. Using $\tau_\kappa = \sqrt{RaPr}\,\tau_{ff}$, this can be expressed in terms of the free-fall time to be $\tau_{drift} \sim 170\,\tau_{ff}$ to $1300\,\tau_{ff}$ for our Ra range of $10^6 < Ra < 6 \times 10^7$. A quantitative measurement of this time scale would require a Fourier time series analysis of even longer data records than the ones we could obtain.

Most experiments on the large-scale flow structure in turbulent RBC use temperature measurements close to the sidewalls of the cell to infer the azimuthal profile of the vertical flow direction from their temperature imprint: up-welling fluid from the hot bottom plate is detected as a high-temperature signal, while down-welling fluid from the cold top plate gives a low-temperature signal. This principle is employed here as well, however at a very fine resolution. Figure 3(b) shows a colour plot of the temperature time series taken simultaneously by 11 thermocouples which are arranged in a semicircle at the sidewall at half-height (see figure 1c). This arrangement allows us to present a space–time plot of the temperature with details never obtained before in a liquid metal flow experiment. Temperatures below the average fluid temperature

$\bar{T}$ are coloured in blue and temperatures above $\bar{T}$ are shown in orange. The black dashed line re-plots the LSC orientation $\theta_{LSC} = (\theta_{top} + 180° + \theta_{bot})/2$ from figure 3(*a*). The profile has been additionally smoothed over time using a moving average filter over five successive measurements. It confirms the coherence of the average LSC: temperature at half-height and velocity dynamics at top/bottom are in perfect synchronization and drift slowly as a common, single LSC roll.

Figures 3(*c*) and 3(*e*) show magnified sections of figure 3(*b*) at finer temporal resolution that correspond to those in figures 3(*f*) and 3(*h*), respectively. In both cases, hot rising and cold falling plumes at the sidewall bounce together and move away from each other again. This periodic motion is known as a sloshing mode of the LSC (Brown & Ahlers 2009; Zhou *et al.* 2009). We detect $\tau_{slosh} = \tau_{osc}$ from these two pairs of panels. Previous experiments in water (Brown & Ahlers 2009; Zhou *et al.* 2009) report that the up- and down-welling flows come as close as 45°. In our measurements this minimal azimuthal distance is much smaller, regularly reaching the order of our azimuthal resolution of 18°. This extreme sloshing amplitude seems to be a property of low-*Pr* convection and the high inertia of liquid metals.

A rare event in the large-scale flow dynamics is shown in figure 3(*d,g*). Here, the LSC rapidly changes its orientation by about 90° within less than $10\tau_{ff}$ ($940 < t/\tau_{ff} < 950$). At the same time, the characteristic sloshing pattern in the temperature plot is disrupted and over most of the circumference the mean value of the temperature is detected which is in line with the absence of the coherent pattern up- or down-welling flow. Only after the sudden orientation change does the sloshing pattern reappear, now shifted by 90° in the azimuthal direction. This observation suggests that a cessation has taken place – an event which has also been observed in experiments in water (Brown & Ahlers 2006) and fluorinert FC-77 electronic liquid (Xie *et al.* 2013). Cessations consist of a breakdown of the coherent LSC into an incoherent flow state and a subsequent re-establishment of the coherence of the LSC with a different orientation. These events are rare; in water experiments they occurred at rates of the order of days^{-1} (Brown & Ahlers 2006; Xie *et al.* 2013). Our measurement series did not reach such time durations. Consequently, a statistical analysis of cessations in the present liquid metal convection experiments was not possible.

In figure 4, two additional experiments – one at the lowest Rayleigh number $Ra = 10^6$ and one at an intermediate $Ra = 10^7$ – are presented. The time series cover again more than 1000 free-fall times in both cases. Just as for $Ra = 6 \times 10^7$ in figure 3, the temperature and velocity measurements show the presence of the LSC, as well as the sloshing and torsion modes in the magnifications. Differences can mainly be seen with respect to the temperature magnitude when comparing the data to figure 3. With increasing *Ra*, the amplitude of the fluid temperature at mid-height of the cell decreases steadily indicating an enhanced mixing of the scalar field due to an increasingly inertial fluid turbulence. Furthermore, the hot and cold patches of the up- and down-wellings are thicker and more washed out for lower Rayleigh numbers. This can be seen best for the lowest $Ra = 10^6$ in figure 4(*d*). We have found that the magnitude of the total long-term azimuthal drift does not show a dependence on the Rayleigh number in the accessible range. To summarize this part, our experimental study shows clearly that the LSC dynamics has to be considered as a superposition of multiple processes with different characteristic time scales which can be reconstructed from the time series.
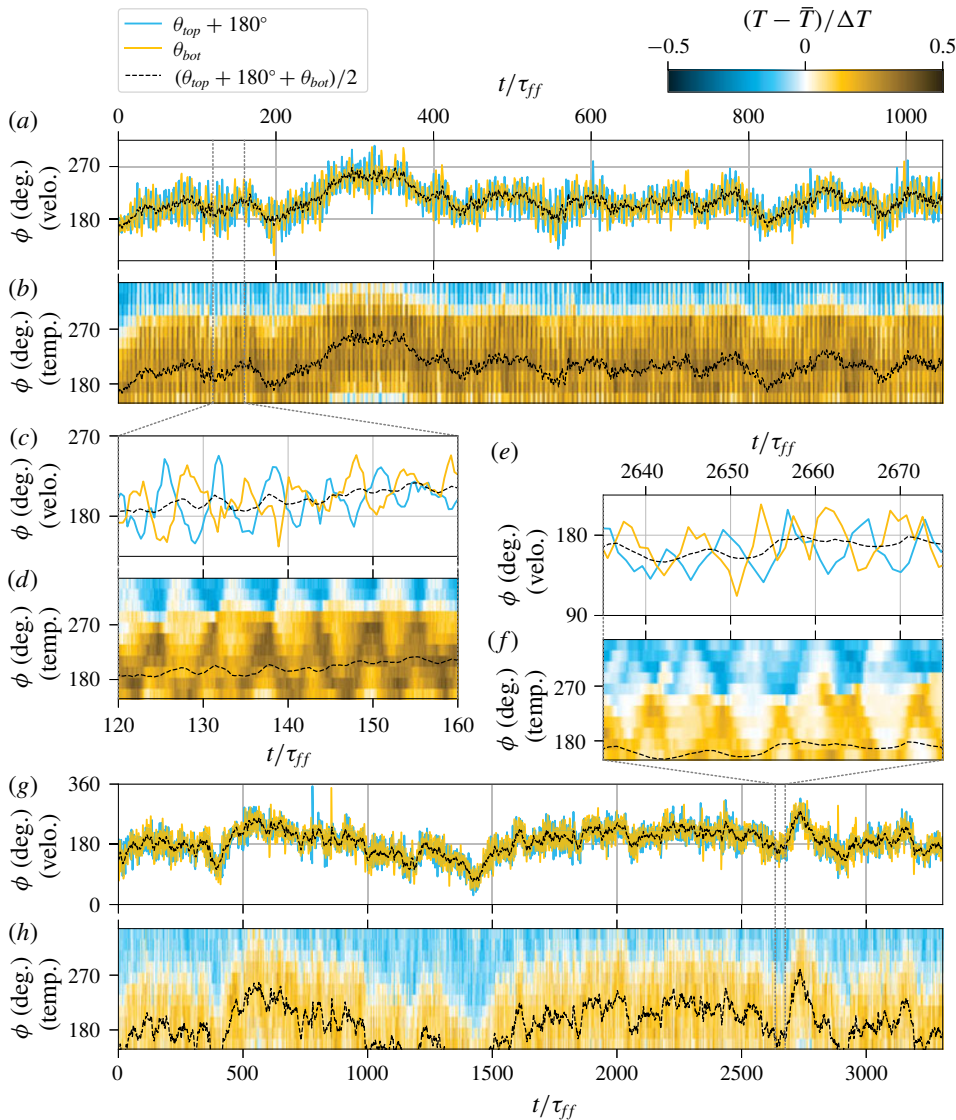
FIGURE 4. Large-scale flow for (*a–d*) $Ra = 10^6$ ($\tau_{ff} = 17$ s) and (*e–h*) $Ra = 10^7$ ($\tau_{ff} = 5.4$ s). Quantities and the colour scale are the same as in figure 3. Panels (*c*) and (*d*) are detailed views of (*a*) and (*b*), respectively. Panels (*e*) and (*f*) are detailed views of (*g*) and (*h*), respectively. The time span of the detailed views is $40\tau_{ff}$.

3.2. *Rayleigh number dependence of oscillation frequencies*

Frequency spectra of θ_{top} are shown for three Rayleigh numbers Ra in figure 5(*a*). A clear peak gives the oscillation frequency f_{osc} of the torsional mode. The characteristic frequency value is extracted by fitting the function $A(f)$ to the spectra

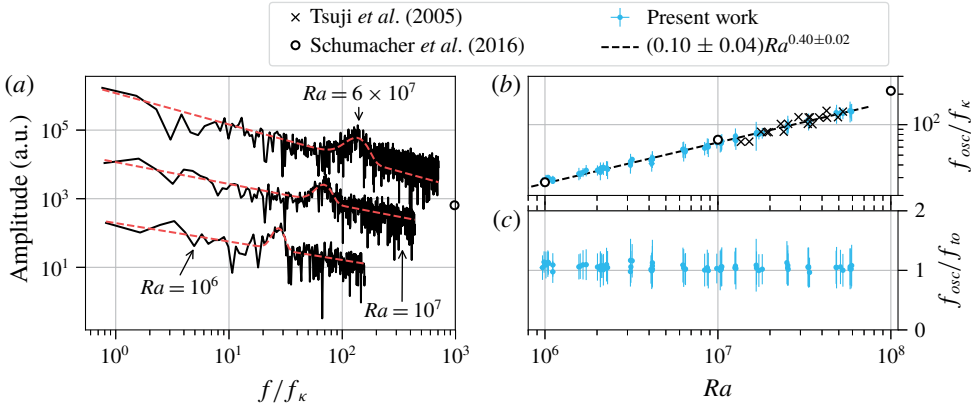$$A(f) = a \exp\left(-\frac{(f - f_{osc})^2}{2\Delta f^2}\right) + bf^{\gamma}. \tag{3.2}$$

FIGURE 5. (Colour online) (a) Frequency spectra of θ_{top} for different Ra, normalized by the thermal diffusion frequency f_κ. The spectra at $Ra = 10^6$ and $Ra = 6 \times 10^7$ are shifted for better visibility by a factor of 0.1 and 20, respectively. The dashed lines are fits of (3.2) to the spectra to determine the characteristic oscillation frequency f_{osc}. (b) Scaling of the frequency f_{osc} with Ra. The error bars are taken from the standard deviation Δf of the Gaussian fit (3.2). (c) Comparison of f_{osc} with the turnover frequency f_{to} over Ra.

This function models the spectra as a Gaussian peak at f_{osc} with a width of Δf on top of an algebraic power-law background. The fitting parameters are a, b, γ, f_{osc} and Δf.

Figure 5(b) shows the Ra dependence of the frequency f_{osc}, normalized by the thermal diffusion frequency

$$f_\kappa = \frac{\kappa}{H^2}. \tag{3.3}$$

The error bars correspond to the standard deviation Δf of the fitted Gaussian peaks. A power law is fitted to the data using orthogonal distance regression (Boggs & Rogers 1990) to incorporate the errors of both the abscissa and the ordinate. The error estimation of the fit is outlined in the Appendix. This procedure is used for all following power-law fits in this work if not noted otherwise. The fit results in a scaling of $f_{osc}/f_\kappa \simeq (0.10 \pm 0.04)Ra^{0.40\pm0.02}$, indicated as a dashed line in figure 5(b). Dimensional arguments suggest a scaling of the oscillation frequency with the free-fall time τ_{ff} of $f_{osc} \propto Ra^{0.5}$ for constant material properties, since $1/\tau_{ff} = \sqrt{\nu\kappa Ra}/H^2$. The exponent of 0.4 indicates that the underlying time scale is indeed close to the free-fall time, but that the inertial character of the fluid turbulence in the low-Prandtl-number flow affects the turbulent momentum transfer. We will return to this point in §4.2.

The DNS by Schumacher *et al.* (2016) at $Pr = 0.021$ result in a slightly stronger scaling of $f_{osc}/f_\kappa \simeq (0.08 \pm 0.05)Ra^{0.42\pm0.02}$ when their data are corrected from radians to units of cycles per diffusive time (open circles in figure 5b). Previous experiments by Tsuji *et al.* (2005) in mercury at a Prandtl number of $Pr = 0.024$ coincide with our results (crosses in figure 5b). For liquid gallium ($Pr = 0.027$) in a $\Gamma = 2$ cell, Vogt *et al.* (2018a) found the same scaling exponent as for the $\Gamma = 1$ case, but with a lower magnitude: $f_{osc}/f_\kappa \simeq 0.027Ra^{0.419\pm0.006}$. The scaling exponents and absolute values for measurements in larger-Prandtl-number fluids are generally higher. For example, in water at $Pr \sim 5.4$ scaling laws of $f_{osc}/f_\kappa \simeq 0.2Ra^{0.46}$ (Qiu & Tong 2001), $f_{osc}/f_\kappa \simeq 0.167Ra^{0.47}$ (Qiu *et al.* 2004) and $f_{osc}/f_\kappa \simeq 0.12Ra^{0.49}$ (Zhou *et al.* 2009) are found. Experiments in methanol at $Pr = 6.0$ (Funfschilling & Ahlers 2004) give a similar

result of $f_{osc}/f_\kappa \simeq 0.126 Ra^{0.460\pm0.012}$. Considering that the thermal diffusivity of water (Çengel 2008) is about 70 times lower than that of GaInSn at 35 °C, the absolute frequencies f_{osc} in water at $Ra = 10^7$ are about 14 times smaller than our values in GaInSn. This higher intensity of the flow dynamics in liquid metals is to be expected, as low-Pr liquids are known to drive a more turbulent convective flow than high-Pr fluids at the same Ra (Breuer *et al.* 2004; Schumacher *et al.* 2015).

The averaged velocity components (3.1) are also used to calculate the velocity amplitude of the LSC:

$$v_{LSC} = \left\langle \frac{|\boldsymbol{v}_{top}| + |\boldsymbol{v}_{bot}|}{2} \right\rangle_t , \tag{3.4}$$

where $\langle \cdot \rangle_t$ denotes a time average. Using this velocity, the turnover time τ_{to} of the LSC can be defined as $\tau_{to} = \pi H/v_{LSC}$. Here, a roll shape in the form of a circle of diameter H has been assumed as the LSC path. The turnover frequency is then

$$f_{to} = \frac{v_{LSC}}{\pi H}. \tag{3.5}$$

Figure 5(*c*) shows the ratio f_{osc}/f_{to}, which is close to unity for all Rayleigh numbers. This implies that one period of the torsional mode – and thus also of the sloshing mode – takes one turnover time of the LSC. If, alternatively, the length $2H + 2D$ is used for the LSC path instead of the circumference of a circle, f_{to} decreases by a factor of $\pi/4 \approx 0.79$. However, the relation of $f_{osc} \propto f_{to}$ would still be valid.

3.3. *Interplay of the torsion and sloshing modes*

In this section, we investigate how the sloshing and torsion modes described in § 3.1 coexist and build a single coherent flow structure. The basic connection of the two modes is that the flow directions at the top and bottom plate, θ_{top} and θ_{bot}, indicate the azimuthal position where the up- and down-welling flows will appear. This can be monitored by the temperature sensors at mid-height. We have already shown that on average the top and bottom flows are anti-parallel with $\langle\theta_{bot}\rangle_t - \langle\theta_{top}\rangle_t \sim 180°$ (see figure 3*a*). If one assumes that these flows will be deflected in different azimuthal directions by an angle $\Delta\theta$ (which represents the effect of the LSC torsion) then the orientation angles will get closer to one another. With $\theta_{top/bot} = \langle\theta_{top/bot}\rangle_t \pm \Delta\theta$, the azimuthal distance of the up- and down-welling flows is given by

$$\theta_{bot} - \theta_{top} \sim 180° - 2\Delta\theta. \tag{3.6}$$

With the torsion displacement $\Delta\theta$ at top and bottom getting closer to 90°, the hot up-welling and cold down-welling flows will also get closer to each other. This is exactly the behaviour of the sloshing mode detected in figure 3(*b*).

However, the flow orientation at the plates and the respective vertical flow at half the height of the cell do not coincide in time. We have established that one oscillation period is the same as one turnover of the LSC. From this point, we would expect that the flow orientation propagates with the same speed, e.g. a given flow direction at the top plate would result in the same azimuthal position of the down-flow a quarter turnover later. To investigate this behaviour more closely, we calculate a temporal correlation of the top and bottom LSC angles with the temperatures measured at mid-height (see figure 6*a*). As an example, we correlate θ_{top} with the cold down-flow at mid-height, which we denote as Top → Cold. All positive values of the temperature
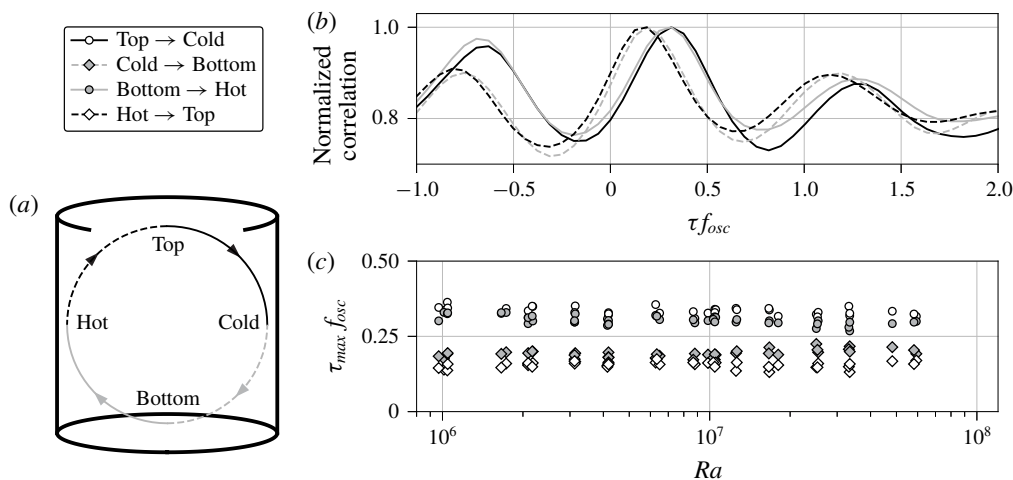
FIGURE 6. Correlation of temperatures at mid-height with flow orientations at the top and bottom plates. (*a*) Illustration of the possible correlations. (*b*) Example of correlations which are normalized by their maxima and plotted over the time shift τ in units of the oscillation frequency f_{osc}. The data record is taken from the measurement in figure 3 at $Ra = 6 \times 10^7$. (*c*) Time shift τ_{max} of the maximal correlation over Ra.

profile are clipped in figure 3(*b*) to zero, in order to include the cold signature of the down-flow only. This is equivalent to clipping the temperatures to the mean fluid temperature $\bar{T}$. Next, we construct a pseudo-temperature profile $\mathcal{T}$ from the time series of θ_{top} which is given by

$$\mathcal{T}(\phi, t) = \begin{cases} A\cos^2(\phi - \theta_{top}(t)), & \text{for } \theta_{top} - 90° < \phi < \theta_{top} + 90°, \\ 0, & \text{else.} \end{cases} \quad (3.7)$$

This profile emulates the temperature at mid-height if the position of the down-flow would follow the flow orientation at the top plate instantaneously. The amplitude is set to $A = -1$ in this particular case since we correlate with the negative values of the measured temperature profile. In the case of a correlation with the up-welling flow, an amplitude $A = 1$ is taken. The function $\mathcal{T}$ is evaluated at the azimuthal positions of the mid-height thermocouples and correlated with the clipped temperature profile over time. The result is normalized by its maximal value and plotted in figure 6(*b*) as a solid black line. The correlation time shift τ is normalized by the oscillation frequency f_{osc}.

We observe that the maximum correlation is shifted to $\tau f_{osc} > 0$, i.e. the down-flow at mid-height lags behind the flow orientation at the top. The time lag τ_{max} of the maximum correlation is calculated by fitting a quadratic polynomial around the maximal value. In the case Top $\rightarrow$ Cold the time shift is $\tau_{max} f_{osc} = 0.32$, which is larger than the expected value of $1/4$. The correlations of the three other cases Cold $\rightarrow$ Bottom, Bottom $\rightarrow$ Hot and Hot $\rightarrow$ Top are displayed in figure 6(*b*) as well. It can be seen that the vertical flows at mid-height have a time lag towards the flows at the respective plate, which is larger than a quarter of one oscillation period (Top $\rightarrow$ Cold and Bottom $\rightarrow$ Hot). Furthermore, the horizontal flows at the plates follow the mid-height flows with a lag shorter than a quarter oscillation period. We repeated this

analysis for all our experiments. The corresponding time shifts display this behaviour (see figure 6c) in all data sets. On average the time lags $\tau_{max} f_{osc}$ are: 0.33 ± 0.01 for Top $\rightarrow$ Cold, 0.19 ± 0.01 for Cold $\rightarrow$ Bottom, 0.30 ± 0.01 for Bottom $\rightarrow$ Hot and 0.16 ± 0.01 for Hot $\rightarrow$ Top. The sum of all four time lags gives on average the expected value of one, here 0.98 ± 0.03, and thus the propagation of the flow orientation requires the same amount of time as one oscillation period or one turnover. From the present data, the flow can be understood as independent parcels of the fluid circulating in the cell. Each fluid parcel circulates on average in a vertical plane which it does not leave. The observed flow modes are then a result of the collective motion of these fluid parcels, which are phase-shifted in time and the azimuthal orientation of their plane. This interpretation of our data does not predict significant azimuthal velocity components as part of the mode dynamics of the LSC. This cannot be verified with the current set-up, but future experiments could aim to include the measurement of azimuthal velocities.

A similar analysis as in figure 6 is found in Qiu *et al.* (2004). Their data reveal a shift close to $\tau_{osc}/4$ between fluctuations of the velocity at the bottom centre and of the temperature at half-height near the up-welling flow. This would correspond to our Bottom $\rightarrow$ Hot case. An exact shift value is however not discernible from their plots. Other data on the phase shift between torsion and sloshing modes can be grouped into three categories: (i) correlation of the top and bottom flow orientations, which gives the characteristic torsion phase shift of $\tau_{osc}/2$; see experiments by Funfschilling & Ahlers (2004) in methanol at $Pr = 6.0$, by Xie *et al.* (2013) in fluorinert FC-77 electronic liquid at $Pr = 19.4$ or by Khalilov *et al.* (2018) in liquid sodium at $Pr = 0.0094$; (ii) correlation of the hot and cold temperature signatures at half-height, resulting in the characteristic sloshing phase shift of $\tau_{osc}/2$; see data by Qiu & Tong (2001) and Xi *et al.* (2009) in water at $Pr \sim 5.3$; and (iii) correlation of the mean LSC orientation at half-height and the top or bottom flow orientation yielding a phase shift of $\tau_{osc}/4$; see measurements by Zhou *et al.* (2009) in water at $Pr = 5.3$. These results are consistent with our data: (i) and (ii) are equivalent to the sum of two successive phase shifts in figure 6 (e.g. Top $\rightarrow$ Cold plus Cold $\rightarrow$ Bottom) and (iii) is equal to an average of two successive phase shifts in figure 6. Each of these analysis steps averages out the deviations of individual time lags from $\tau_{osc}/4$ and results in phase shifts of $\tau_{osc}/2$ for (i) and (ii), and $\tau_{osc}/4$ for (iii). All these data show that the torsion and sloshing modes are present for a wide range of Prandtl numbers. However, whether the specific time lags found in our system are a general feature needs to be clarified in the future.

The deviations of the individual lags from a quarter oscillation period indicate that the LSC path is asymmetric. Such distortions might be caused by corner vortices of the LSC which are observed in simulations. Here, we introduce a horizontal axis ξ that is aligned in the direction of the LSC orientation. To calculate an averaged horizontal velocity profile of the LSC at the top (bottom) plate, we select the velocity profiles of the UDV sensors T_0, T_{45} and T_{90} (B_0, B_{45} and B_{90}) at time instants when the LSC orientation θ_{top} (θ_{bot}) is aligned within $\pm 5°$ with the azimuthal position of a sensor. The averages of those velocity profiles $\bar{v}_\xi(\xi)$ are normalized by their maximum magnitude and shown in figure 7 for three different Ra. It should be noted that the noisy or missing profiles for $\xi > 80$ mm are due to an inaccessible zone close to the UDV sensors caused by the ringing of the piezo-crystal in the transducer. The velocities at the top plate are predominantly positive (flow to the right) and the bottom velocities are negative (flow to the left). Inverted velocities can only be seen at the positions where the up- and down-welling flows are impinging on the plates
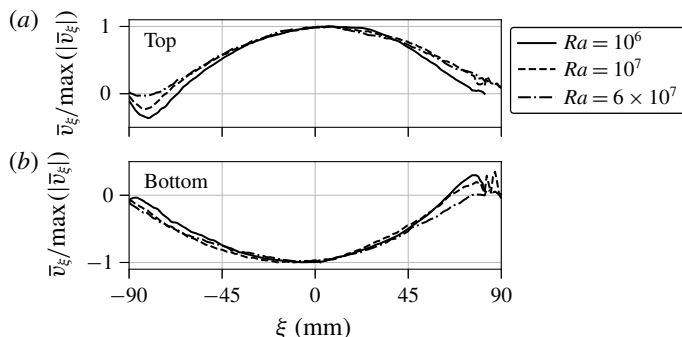
FIGURE 7. Averaged and normalized horizontal UDV velocity profiles along the LSC at (*a*) the top and (*b*) the bottom plate for different *Ra*. The experiments correspond to the ones shown in figure 5(*a*).

(left at the top, right at the bottom). These profiles indicate indeed the presence of recirculation vortices in the cell corners, which seem to become smaller with increasing *Ra*. This challenges our supposition at the beginning of this paragraph that corner vortices might be responsible for the different time lags in figure 6(*c*). With increasing Rayleigh number the fluid turbulence becomes more vigorous. This means that the vortical structures are still there, but get averaged out more effectively.

A further explanation for the phase-shift deviations from the expected value of $\tau_{osc}/4$ could be traced to a varying LSC velocity. The fluid would have to be slower when leaving the plates (Top → Cold and Bottom → Hot) and accelerate while approaching the opposite plate (Cold → Bottom and Hot → Top). This point has to be left for future studies on this subject.

4. Turbulent transport of momentum and heat

4.1. *Heat transport*

This section discusses the global transport properties in the liquid metal convection flow and compares the results with other experiments and simulations. We first analyse the turbulent heat transport in the experiment. The heat flux through the fluid layer is characterized by the Nusselt number *Nu* which is calculated at the cooled plate, $Nu = \dot{Q}/\dot{Q}_{cond}$. Here, $\dot{Q}_{cond} = \lambda \pi R^2 \Delta T/H$ is the purely conductive heat flux. The data are plotted over *Ra* in figure 8 and we find $Nu \simeq (0.12 \pm 0.04)Ra^{0.27\pm0.02}$. This agrees excellently with measurements by Cioni *et al.* (1997) in mercury ($Pr = 0.025$) and matches the numerical results of Scheel & Schumacher (2017) of $Nu \simeq (0.13 \pm 0.04)Ra^{0.27\pm0.01}$ for $Pr = 0.021$ with only a small shift.

The results of Takeshita *et al.* (1996) in mercury ($Pr = 0.024$) agree with respect to the scaling exponent, but give a somewhat higher Nusselt number magnitude with $Nu \simeq 0.155Ra^{0.27\pm0.02}$. King & Aurnou (2013, 2015) found the same magnitude of *Nu* in gallium ($Pr \sim 0.025$), but their scaling exponent is smaller, $Nu \simeq (0.19 \pm 0.01)Ra^{0.249\pm0.004}$. All of the above experiments and simulations were conducted in cylindrical cells with $\Gamma = 1$. Finally, Glazier *et al.* (1999) conducted experiments in mercury ($Pr \sim 0.025$) for multiple aspect ratios. Their data at $\Gamma = 1$ are closer to the results of Takeshita *et al.* (1996) in magnitude (see figure 8). A least-squares fit gives a slower scaling $Nu \propto Ra^{0.242\pm0.002}$ in the considered range. Including all their data for $\Gamma = 0.5$ and 2, they found a scaling $Nu \propto Ra^{0.29\pm0.01}$ over a
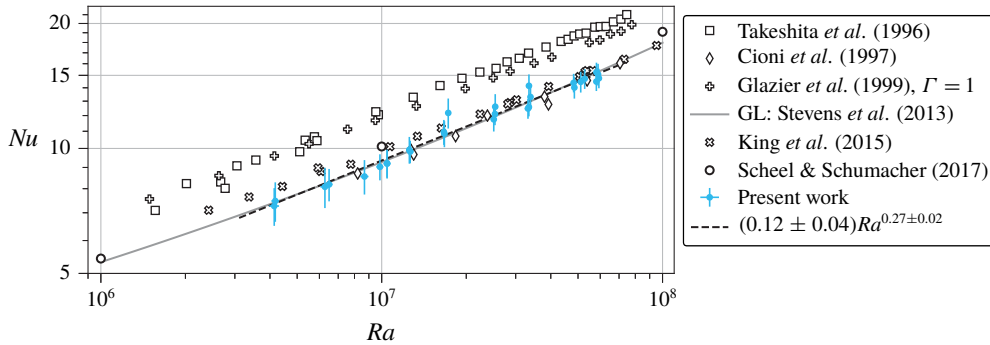
FIGURE 8. (Colour online) Turbulent heat transfer in liquid metal convection flow. The scaling of Nu versus Ra is displayed. The Nusselt number Nu is determined from the temperature difference of the cooling water for $T_{out} - T_{in} > 0.2$ K. Our data are compared with a numerical simulation (circles), four laboratory experiments and the GL theory at $Pr = 0.029$, as indicated in the legend.

large range of $10^5 < Ra < 10^{11}$. The deviation of their $\Gamma = 1$ data from this exponent is attributed to a strong bulk circulation.

The Grossmann–Lohse (GL) theory prediction (Stevens *et al.* 2013) is in very good agreement with our data as seen by the grey line in figure 8. It can also be seen that the GL theory predicts an increase in the exponent of $Nu(Ra)$ for higher Ra. At smaller Rayleigh numbers ($Ra \lesssim 5 \times 10^5$), Rossby (1969) found $Nu \simeq 0.147 Ra^{0.257 \pm 0.004}$ for $Pr = 0.025$ and $\Gamma \sim 22$ and 7.4. Kek & Müller (1993) reported $Nu \simeq 0.20 Ra^{0.20}$ at $Pr = 0.006$ and $\Gamma \sim 11$.

4.2. *Momentum transport*

The turbulent momentum transport of the convection flow is quantified by the Reynolds number Re. In contrast to the quantification of the turbulent heat transfer by a Nusselt number, the Reynolds number is not uniquely defined since different characteristic velocities can be employed for its definition. With the multiple probes at hand, we can define three different Re with three different corresponding characteristic velocities: (1) the typical horizontal velocity magnitude near the plates, (2) the typical vertical velocity magnitude of the LSC along the sidewall and (3) the turbulent velocity fluctuations in the centre of the cell,

$$Re_{LSC} = \frac{v_{LSC} H}{\nu}, \quad Re_{vert} = \frac{v_{vert} H}{\nu} \quad \text{and} \quad Re_{centre} = \frac{v_{centre} H}{\nu}. \quad (4.1a-c)$$

This circumstance gives the opportunity to directly compare the sensitivity of the scaling exponent with respect to these different characteristic velocities.

First, the large-scale flow is characterized by the velocity magnitude v_{LSC} as done in § 3.2. The resulting Reynolds number $Re_{LSC} = v_{LSC} H/\nu$ is plotted in figure 9 (filled circles). A power-law fit reveals a scaling of $Re_{LSC} \simeq (8.0 \pm 4.4) Ra^{0.42 \pm 0.03}$. The exponent is close to the scaling of f_{to} and f_{osc} in figure 5(b) since $Re_{LSC} = f_{to} \pi H^2/\nu$.

Second, the vertical velocity of the LSC is measured at radial position $r/R = 0.8$ by the UDV sensor V_0. Due to the sloshing mode, the up- or down-welling flows move periodically towards and away from the sensor measuring volume (see figure 9b).
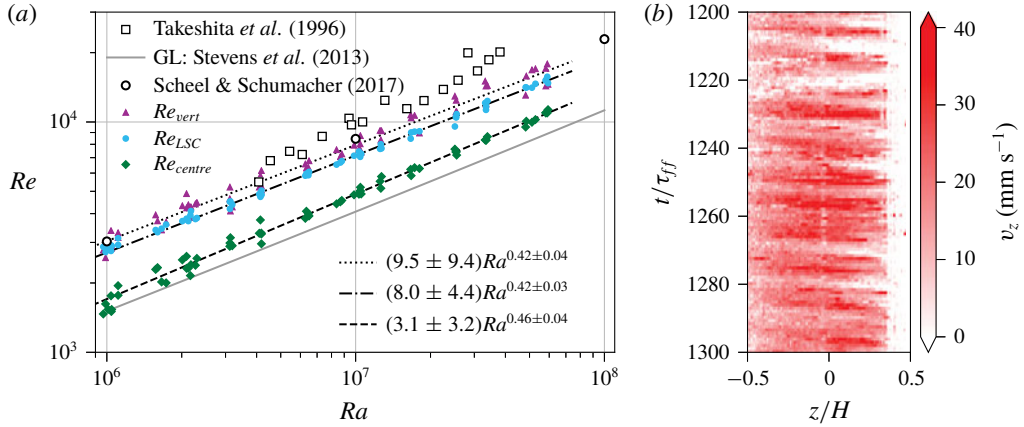
FIGURE 9. (Colour online) Analysis of the turbulent momentum transfer in liquid metal convection flow based on the present UDV measurements. (*a*) Scaling of Reynolds number Re with Rayleigh number Ra. Uncertainties of the present measurements were removed for better visibility. Their relative values are about 20 % to 30 % due to the turbulent fluctuations. (*b*) Colour-plot of v_z measured by UDV sensor V_0 for $Ra = 6 \times 10^7$. The data correspond to the measurement shown in figure 3.

Additionally, the LSC is slowly rotating as a whole. Since a pronounced vertical flow of the LSC is of interest only, we estimate the characteristic vertical velocity by calculating the average velocity profile $v_z(t)$ over an interval $H/4$ centred around the mid-plane for every time step, similar to (3.1). The corresponding standard deviation (std) is added to the average of the resulting velocity magnitude to accommodate for the fluctuations of this signal. Thus, $v_{vert} = \langle |v_z(t)| \rangle_t + \mathrm{std}(|v_z(t)|)$. This velocity gives a vertical Reynolds number $Re_{vert} = v_{vert}H/\nu$. The values are shown in figure 9(*a*) as triangles and give a scaling of $Re_{vert} \simeq (9.5 \pm 9.4)Ra^{0.42 \pm 0.04}$.

Finally, the turbulent velocity fluctuations are considered in the centre of the cell. Here, the three crossing UDV sensors M_0, M_{90} and V_c can measure all three components of the velocity vector $\boldsymbol{v}_{centre}$ (see figure 1*b*). The components are determined by taking the root-mean-square (r.m.s.) value of, again, the central $H/4$ interval of the velocity profiles. The r.m.s. time average of the velocity magnitude $v_{centre} = \langle (\boldsymbol{v}_{centre}(t))^2 \rangle_t^{1/2}$ is used to calculate $Re_{centre} = v_{centre}H/\nu$. It is plotted as diamonds in figure 9(*a*), along with the power-law fit of $Re_{centre} \simeq (3.1 \pm 3.2)Ra^{0.46 \pm 0.04}$.

The scaling exponent of $Re_{centre}(Ra)$ agrees very well with the result of DNS by Scheel & Schumacher (2017) (open circles in figure 9*a*). In the numerical simulations, the Reynolds number was calculated from the r.m.s. velocity over the whole cell for $Pr = 0.021$ and gave a scaling of $Re \simeq (6.5 \pm 0.6)Ra^{0.45 \pm 0.01}$. The absolute values of Re_{centre} are about half as large as the results of the DNS, since the average over the whole cell volume also includes the high-velocity components of the LSC outside the centre region. The absolute values of Re_{LSC} and Re_{vert} match the DNS results more closely, but have a somewhat smaller exponent of 0.42.

How do our results compare to previous laboratory experiments? Measurements of a vertical Reynolds number in mercury by Takeshita *et al.* (1996) were also taken at half-height and $r/R = 0.8$. They show a higher velocity magnitude with a scaling of $Re \simeq 6.24Ra^{0.46 \pm 0.02}$. In the $\Gamma = 2$ case, Vogt *et al.* (2018*a*) found an increased scaling exponent for a horizontal Re at the cell centre: $Re \simeq 5.662Ra^{0.483}$. Comparing

all these results underlines the dependence of the momentum transport on the specific velocity that enters the Reynolds number definition. The somewhat smaller scaling exponent for the horizontal and vertical LSC velocities in comparison to previous experiments or the DNS can thus be considered as a result of probing different parts of the complex three-dimensional flow structure that we analysed before, as well as using different measurement techniques and procedures of calculating the characteristic velocities. Interestingly, the turbulent fluctuations seem to be the best indication of the global momentum transport scaling as reported by DNS, albeit being smaller in their absolute magnitude.

We also show the Reynolds number predicted by the GL theory (Stevens *et al.* 2013) in figure 9*a*. Compared to Re_{LSC} and Re_{vert}, the GL theory underpredicts the Reynolds number by up to a factor of 2. Stevens *et al.* (2013) used here a measurement at $Pr = 5.4$ to fix the values of Re. A least-squares power-law fit of the GL results in figure 9*a* gives an exponent of $Re \propto Ra^{0.44}$, which lies within the accuracy of our experimental data.

5. Small-scale flow structure in the centre of the convection cell

The UDV measurements in liquid metal convection monitor the longitudinal velocity profile along the beam line. This opens the possibility of analysing the statistics of longitudinal velocity increments directly and thus the small-scale statistics in the bulk of a liquid metal flow (see Lohse & Xia (2010) for a comprehensive review). We consider longitudinal velocity increments which are given by $\delta_r v(t) = [v(x + r, t) - v(x, t)] \cdot r/r$, with $r = |r|$. The velocity profiles v are measured by the UDV sensors M_0, M_{90} and V_c. Vertical velocity profiles $v_z(z, t)$ are taken directly from the UDV sensor V_c. Horizontal velocity profiles, however, have to be considered in their relation to the LSC orientation. In line with the discussion in § 3.3, we collect the velocity profiles $v_\xi(\xi, t)$ of the UDV sensors M_0 and M_{90} when the mean LSC orientation angle θ_{LSC} is aligned within $\pm 5°$ with the beam line of these sensors. Additionally, we introduce a horizontal axis η, which is perpendicular to the LSC orientation and collect the horizontal velocity profiles $v_\eta(\eta, t)$ from M_0 and M_{90} when $\theta_{LSC} + 90°$ is aligned with the sensors. The analysis is thus conditioned to the LSC orientation.

In order to quantify the degree of isotropy of the velocity fluctuations in the turbulent flow, we start with a comparison of the longitudinal second-order structure functions or velocity increment moments which are given by

$$S_i(r) = \langle (\delta_r v_i)^2 \rangle_{x,t}, \quad \text{with } r = r e_i, \tag{5.1}$$

and $i = \xi, \eta, z$. The average is taken with respect to time and to points along the beam line. Table 1 shows the mutual ratios of these moments for three distances $\tilde{r} = r/R$ with R being the cell radius. Approximate isotropy would follow when these ratios are very close to unity. Our data clearly indicate that this is not the case, particularly for the smallest separation. The data suggest that the LSC flow is responsible for these deviations and affects the fluctuations over a wide range of scales. The present Rayleigh numbers are small in comparison to the measurements by Mashiko *et al.* (2004) at $Pr = 0.024$, by Sun, Zhou & Xia (2006) at $Pr = 4.3$ or the DNS by Kunnen *et al.* (2008) at $Pr = 4$, such that we cannot present a scaling analysis of the second-order structure function.

Figure 10 shows the probability density functions (p.d.f.) of the normalized vertical velocity increment $\tilde{\delta}_r v_z = \delta_r v_z / \langle \delta_r v_z \rangle_{rms}$ for the same separations $\tilde{r}$ and Rayleigh
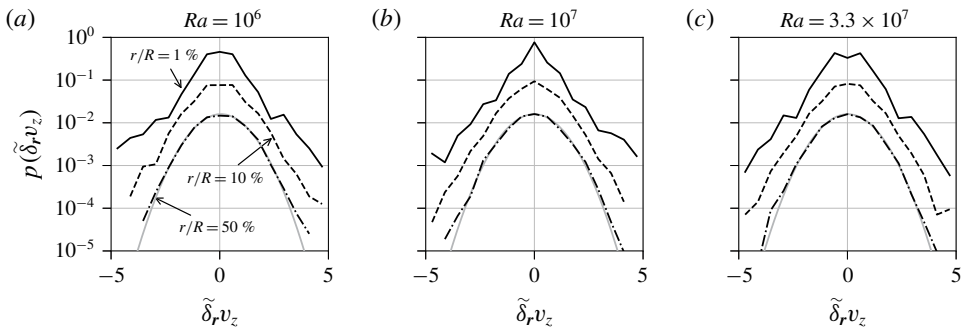
FIGURE 10. The p.d.f. of the normalized velocity increments $\tilde{\delta}_r v_z$, calculated from the UDV sensor V_c, for different Rayleigh numbers (*a–c*). The styles of the black lines correspond to the spatial increment r as specified in (*a*). The p.d.f. for higher r are successively shifted by a factor of 0.2 for better visibility. The grey line is a normal distribution with mean and variance of the p.d.f. for $r/R = 50\%$.

	$Ra = 10^6$			$Ra = 10^7$			$Ra = 3.3 \times 10^7$		
$\tilde{r} = \dfrac{r}{R}$	$\dfrac{S_\xi(\tilde{r})}{S_z(\tilde{r})}$	$\dfrac{S_\eta(\tilde{r})}{S_z(\tilde{r})}$	$\dfrac{S_\eta(\tilde{r})}{S_\xi(\tilde{r})}$	$\dfrac{S_\xi(\tilde{r})}{S_z(\tilde{r})}$	$\dfrac{S_\eta(\tilde{r})}{S_z(\tilde{r})}$	$\dfrac{S_\eta(\tilde{r})}{S_\xi(\tilde{r})}$	$\dfrac{S_\xi(\tilde{r})}{S_z(\tilde{r})}$	$\dfrac{S_\eta(\tilde{r})}{S_z(\tilde{r})}$	$\dfrac{S_\eta(\tilde{r})}{S_\xi(\tilde{r})}$
0.01	0.56	0.30	0.53	0.77	0.38	0.49	0.83	0.69	0.83
0.10	0.98	0.77	0.79	1.15	0.82	0.71	1.13	0.93	0.83
0.50	0.82	1.01	1.23	1.03	0.90	0.88	0.99	0.93	0.93

TABLE 1. Comparison of second-order structure functions (or second-order velocity increment moments) evaluated at three distances in the centre of the convection cell for different directions. Ratios of the vertical structure function $S_z(\tilde{r})$, the horizontal structure function parallel to the LSC $S_\xi(\tilde{r})$ and the horizontal structure function perpendicular to the LSC $S_\eta(\tilde{r})$ are analysed. The table lists the ratios of the horizontal to the vertical values as well as the ratio of both horizontal function values. The data are given for three Rayleigh numbers Ra. The spatial distance r is given in units of the convection cell radius R and $\tilde{r} = r/R$.

numbers Ra as in table 1. We have verified that the quantitative behaviour of the corresponding p.d.f. of $\tilde{\delta}_r v_\xi$ and $\tilde{\delta}_r v_\eta$ is the same (and thus not displayed). For all values of Ra, the p.d.f. approaches a normal distribution with increasing increment size, a result that is well known from homogeneous isotropic turbulence (see e.g. the DNS by Gotoh, Fukayama & Nakano (2002)). For the smallest separation, the p.d.f. is characterized by exponential tails. Even though we were not able to resolve far tails of the p.d.f., which are stretched exponential, our distributions reflect an intermittent, fully developed fluid turbulence in the bulk of the cell.

6. Conclusion

We presented an analysis of turbulent liquid metal convection in a cylindrical cell with aspect ratio $\Gamma = 1$. The combination of multiple UDV and temperature measurements allowed us to reconstruct and characterize essential features of the three-dimensional LSC in the cell experimentally. The dynamics of the LSC is a

superposition of different dynamical processes on different time scales. The slow meandering of the large-scale flow orientation in the closed cell proceeds at a scale of the order of up to 10^3 free-fall time units in the present parameter range – a time scale that is not accessible in DNS at such low Prandtl numbers. The torsional and sloshing modes of the LSC, which are known from studies in water, could be detected by velocity and temperature measurements in the present low-*Pr* experiment. We find a very synchronous sloshing at a time scale of $10\tau_{ff}$ that suggests a more coherent large-scale flow as for higher *Pr*. This time scale is consistent with temperature measurements of previous experiments in mercury (Tsuji *et al.* 2005) and recent DNS (Schumacher *et al.* 2016). It also coincides with the turnover time of the LSC. The temporal correlations between different segments of the LSC, which we verified by combination of velocity and temperature measurements, are nearly independent of the Rayleigh number. Cessations of the large-scale flow remain rare events in the low-Prandtl-number convection regime. In summary, our analysis supports the picture of a very coherent large-scale flow in the closed cell for turbulent convection at such low Prandtl number.

The turbulent momentum transport was determined in multiple ways in the cell by direct velocity measurements. Depending on the UDV beam-line position with respect to the large-scale flow, the resulting *Re* can vary in amplitude by a factor of two or even more. The scaling behaviour with respect to the Rayleigh number is found to agree well with previous studies. The same holds for the turbulent heat transfer. The present ultrasound measurements of velocity increments reveal an inertial fluid turbulence in the bulk, e.g. by extended tails of the distribution of small-separation increments. We also showed that the coherent large-scale flow seems to prevent the establishment of local isotropy in the bulk, a point that might be worth deeper exploration in simulations, in particular for larger aspect ratios.

Our study is based to a large extent on direct velocity field measurements in liquid metal flow. Even though several of the properties that we discussed are known from convective turbulence in air or water, one value of this work is to demonstrate these features in an opaque liquid metal flow. Differences of the presented data with respect to data obtained in water or air are: (i) a more coherent dynamics of the LSC and (ii) large-scale flow oscillations with higher frequencies and amplitudes, most probably due to the higher inertia of fluid turbulence in liquid metal flows. The latter point is also apparent in the higher amplitudes of the mean global momentum transfer. Experimental investigations of liquid metal convection become even more important once they are pushed to higher Rayleigh numbers in GaInSn or to even lower Prandtl numbers in liquid sodium. In those parameter ranges, the total integration times in DNS will be even shorter since the time-step width is ultimately limited by the strong temperature diffusion. Given that in our case the thermal diffusion time has values of $170\,\tau_{ff}$ to $1300\,\tau_{ff}$, experiments of the present kind are currently the only way to study longer-term evolutions in these convection flows.

Supplementary material

Supplementary material is available at https://doi.org/10.1017/jfm.2019.556.

Appendix

In this work, power-law fits to data with errors on both the abscissa and the ordinate are conducted using orthogonal distance regression (Boggs & Rogers 1990). To evaluate the accuracy of the resulting amplitude and exponent values, the fit is repeated multiple times while varying the measurement points randomly according to their uncertainties, which are assumed to be normally distributed. This results in histograms of the amplitude and exponent, which converge to a constant distribution for a high enough number of repetitions. The parameter errors are the standard deviations of these distributions with respect to the initial orthogonal distance regression results. The exponent histogram converges to a Gaussian distribution. The amplitude, however, can be understood in terms of an inverse Gaussian distribution, which allows for positive values only. This procedure was adopted here in order to more accurately include the effect of the data uncertainty on the accuracy of scaling exponents.

REFERENCES

ADRIAN, R. J. & WESTERWEEL, J. 2011 *Particle Image Velocimetry*. Cambridge University Press.

AHLERS, G., GROSSMANN, S. & LOHSE, D. 2009 Heat transfer and large scale dynamics in turbulent Rayleigh–Bénard convection. *Rev. Mod. Phys.* **81** (2), 503–537.

BOGGS, P. T. & ROGERS, J. E. 1990 Orthogonal distance regression. In *Statistical Analysis of Measurement Error Models and Applications*, Contemporary Mathematics, vol. 112, pp. 183–194. American Mathematical Society.

BREUER, M., WESSLING, S., SCHMALZL, J. & HANSEN, U. 2004 Effect of inertia in Rayleigh–Bénard convection. *Phys. Rev.* E **69** (2), 026302.

BROWN, E. & AHLERS, G. 2006 Rotations and cessations of the large-scale circulation in turbulent Rayleigh–Bénard convection. *J. Fluid Mech.* **568**, 351–386.

BROWN, E. & AHLERS, G. 2009 The origin of oscillations of the large-scale circulation of turbulent Rayleigh–Bénard convection. *J. Fluid Mech.* **638**, 383–400.

ÇENGEL, Y. A. 2008 *Introduction to Thermodynamics and Heat Transfer*, 2nd edn. McGraw-Hill Primis.

CHILLÀ, F. & SCHUMACHER, J. 2012 New perspectives in turbulent Rayleigh–Bénard convection. *Eur. Phys. J.* E **35** (7), 58.

CHRISTENSEN, U. R. & AUBERT, J. 2006 Scaling properties of convection-driven dynamos in rotating spherical shells and application to planetary magnetic fields. *Geophys. J. Int.* **166** (1), 97–114.

CIONI, S., CILIBERTO, S. & SOMMERIA, J. 1997 Strongly turbulent Rayleigh–Bénard convection in mercury: comparison with results at moderate Prandtl number. *J. Fluid Mech.* **335**, 111–140.

FRANKE, S., LIESKE, H., FISCHER, A., BÜTTNER, L., CZARSKE, J. W., RÄBIGER, D. & ECKERT, S. 2013 Two-dimensional ultrasound Doppler velocimeter for flow mapping of unsteady liquid metal flows. *Ultrasonics* **53** (3), 691–700.

FUNFSCHILLING, D. & AHLERS, G. 2004 Plume Motion and Large-Scale Circulation in a Cylindrical Rayleigh–Bénard Cell. *Phys. Rev. Lett.* **92** (19), 194502.

GLAZIER, J. A., SEGAWA, T., NAERT, A. & SANO, M. 1999 Evidence against 'ultrahard' thermal turbulence at very high Rayleigh numbers. *Nature* **398**, 307–310.

GOTOH, T., FUKAYAMA, D. & NAKANO, T. 2002 Velocity field statistics in homogeneous steady turbulence obtained using a high-resolution direct numerical simulation. *Phys. Fluids* **14** (3), 1065–1081.

HOYER, K., HOLZNER, M., LÜTHI, B., GUALA, M., LIBERZON, A. & KINZELBACH, W. 2005 3D scanning particle tracking velocimetry. *Exp. Fluids* **39** (5), 923–934.

KEK, V. & MÜLLER, U. 1993 Low Prandtl number convection in layers heated from below. *Int. J. Heat Mass Transf.* **36** (11), 2795–2804.

KELLEY, D. H. & WEIER, T. 2018 Fluid mechanics of liquid metal batteries. *Appl. Mech. Rev.* **70** (2), 020801.

KHALILOV, R., KOLESNICHENKO, I., PAVLINOV, A., MAMYKIN, A., SHESTAKOV, A. & FRICK, P. 2018 Thermal convection of liquid sodium in inclined cylinders. *Phys. Rev. Fluids* **3** (4), 043503.

KING, E. M. & AURNOU, J. M. 2013 Turbulent convection in liquid metal with and without rotation. *Proc. Natl Acad. Sci. USA* **110** (17), 6688–6693.

KING, E. M. & AURNOU, J. M. 2015 Magnetostrophic balance as the optimal state for turbulent magnetoconvection. *Proc. Natl Acad. Sci. USA* **112** (4), 990–994.

KUNNEN, R. P. J., CLERCX, H. J. H., GEURTS, B. J., VAN BOKHOVEN, L. J. A., AKKERMANS, R. A. D. & VERZICCO, R. 2008 Numerical and experimental investigation of structure-function scaling in turbulent Rayleigh–Bénard convection. *Phys. Rev.* E **77** (1), 016302.

LOHSE, D. & XIA, K.-Q. 2010 Small-scale properties of turbulent Rayleigh–Bénard convection. *Annu. Rev. Fluid Mech.* **42** (1), 335–364.

MASHIKO, T., TSUJI, Y., MIZUNO, T. & SANO, M. 2004 Instantaneous measurement of velocity fields in developed thermal turbulence in mercury. *Phys. Rev.* E **69** (3), 036306.

MÜLLER, U. & BÜHLER, L. 2001 *Magnetofluiddynamics in Channels and Containers*. Springer.

PLEVACHUK, Y., SKLYARCHUK, V., ECKERT, S., GERBETH, G. & NOVAKOVIC, R. 2014 Thermophysical properties of the liquid Ga–In–Sn eutectic alloy. *J. Chem. Engng Data* **59** (3), 757–763.

QIU, X.-L., SHANG, X.-D., TONG, P. & XIA, K.-Q. 2004 Velocity oscillations in turbulent Rayleigh–Bénard convection. *Phys. Fluids* **16** (2), 412–423.

QIU, X.-L. & TONG, P. 2001 Onset of coherent oscillations in turbulent Rayleigh–Bénard convection. *Phys. Rev. Lett.* **87** (9), 094501.

ROSSBY, H. T. 1969 A study of Bénard convection with and without rotation. *J. Fluid Mech.* **36** (2), 309–335.

SALAVY, J.-F., BOCCACCINI, L. V., LÄSSER, R. L., MEYDER, R., NEUBERGER, H., POITEVIN, Y., RAMPAL, G., RIGAL, E., ZMITKO, M. & AIELLO, A. 2007 Overview of the last progresses for the European Test Blanket Modules projects. *Fusion Engng Des.* **82** (15), 2105–2112.

SCHEEL, J. D. & SCHUMACHER, J. 2016 Global and local statistics in turbulent convection at low Prandtl numbers. *J. Fluid Mech.* **802**, 147–173.

SCHEEL, J. D. & SCHUMACHER, J. 2017 Predicting transition ranges to fully turbulent viscous boundary layers in low Prandtl number convection flows. *Phys. Rev. Fluids* **2** (12), 123501.

SCHUMACHER, J., BANDARU, V., PANDEY, A. & SCHEEL, J. D. 2016 Transitional boundary layers in low-Prandtl-number convection. *Phys. Rev. Fluids* **1** (8), 084402.

SCHUMACHER, J., GÖTZFRIED, P. & SCHEEL, J. D. 2015 Enhanced enstrophy generation for turbulent convection in low-Prandtl-number fluids. *Proc. Natl Acad. Sci. USA* **112** (31), 9530–9535.

SCHUMACHER, J. & SCHEEL, J. D. 2016 Extreme dissipation event due to plume collision in a turbulent convection cell. *Phys. Rev.* E **94** (4), 043104.

SHI, N., EMRAN, M. S. & SCHUMACHER, J. 2012 Boundary layer structure in turbulent Rayleigh–Bénard convection. *J. Fluid Mech.* **706**, 5–33.

SPIEGEL, E. A. 1962 Thermal turbulence at very small Prandtl number. *J. Geophys. Res.* **67** (8), 3063–3070.

STEVENS, R. J. A. M., CLERCX, H. J. H. & LOHSE, D. 2011 Effect of plumes on measuring the large scale circulation in turbulent Rayleigh–Bénard convection. *Phys. Fluids* **23** (9), 095110.

STEVENS, R. J. A. M., VAN DER POEL, E. P., GROSSMANN, S. & LOHSE, D. 2013 The unifying theory of scaling in thermal convection: the updated prefactors. *J. Fluid Mech.* **730**, 295–308.

SUN, C., XIA, K.-Q. & TONG, P. 2005 Three-dimensional flow structures and dynamics of turbulent thermal convection in a cylindrical cell. *Phys. Rev.* E **72** (2), 026302.

SUN, C., ZHOU, Q. & XIA, K.-Q. 2006 Cascades of velocity and temperature fluctuations in buoyancy-driven thermal turbulence. *Phys. Rev. Lett.* **97** (14), 144504.

TAKEDA, Y. 1987 Measurement of velocity profile of mercury flow by ultrasound Doppler shift method. *Nucl. Technol.* **79** (1), 120–124.

TAKESHITA, T., SEGAWA, T., GLAZIER, J. A. & SANO, M. 1996 Thermal turbulence in mercury. *Phys. Rev. Lett.* **76** (9), 1465.

TOSCHI, F. & BODENSCHATZ, E. 2009 Lagrangian properties of particles in turbulence. *Annu. Rev. Fluid Mech.* **41** (1), 375–404.

TSUJI, Y., MIZUNO, T., MASHIKO, T. & SANO, M. 2005 Mean wind in convective turbulence of mercury. *Phys. Rev. Lett.* **94** (3), 034501.

VAN DER POEL, E. P., STEVENS, R. J. A. M. & LOHSE, D. 2013 Comparison between two- and three-dimensional Rayleigh–Bénard convection. *J. Fluid Mech.* **736**, 177–194.

VOGT, T., HORN, S., GRANNAN, A. M. & AURNOU, J. M. 2018a Jump rope vortex in liquid metal convection. *Proc. Natl Acad. Sci. USA* **115** (50), 12674–12679.

VOGT, T., ISHIMI, W., YANAGISAWA, T., TASAKA, Y., SAKURABA, A. & ECKERT, S. 2018b Transition between quasi-two-dimensional and three-dimensional Rayleigh–Bénard convection in a horizontal magnetic field. *Phys. Rev. Fluids* **3** (1), 013503.

XI, H.-D., ZHOU, S.-Q., ZHOU, Q., CHAN, T.-S. & XIA, K.-Q. 2009 Origin of the temperature oscillation in turbulent thermal convection. *Phys. Rev. Lett.* **102** (4), 044503.

XIE, Y.-C., WEI, P. & XIA, K.-Q. 2013 Dynamics of the large-scale circulation in high-Prandtl-number turbulent thermal convection. *J. Fluid Mech.* **717**, 322–346.

ZHOU, Q., XI, H.-D., ZHOU, S.-Q., SUN, C. & XIA, K.-Q. 2009 Oscillations of the large-scale circulation in turbulent Rayleigh–Bénard convection: the sloshing mode and its relationship with the torsional mode. *J. Fluid Mech.* **630**, 367–390.